International Journal of Multiphase Flow 205 (2026) 105969

Contents lists available at ScienceDirect

International Journal of Multiphase Flow

journal homepage: www.elsevier.com/locate/ijmulflow

Research Paper

Pulsating primary breakup in dual gas-assisted annular liquid sheets

Juliana Richter [a,*], Julia Roeb [a,b], Tobias Jakobs [a], Frederik Scheiff [a,c], Oliver T. Stein [b], Thomas Kolb [a,c]

[a] Institute for Technical Chemistry, Hermann-von-Helmholtz-Platz 1, Eggenstein-Leopoldshafen, 76344, Germany
[b] Engler-Bunte-Institut, Simulation of Reacting Thermo-Fluid Systems, Engler-Bunte-Ring 7, Karlsruhe, 76131, Germany
[c] Engler-Bunte-Institut, Fuel Technology, Engler-Bunte-Ring 7, Karlsruhe, 76131, Germany

ARTICLE INFO

Keywords:
Sheet atomization
Pulsation
Frequency
Primary breakup
CFD
VOF-LES

ABSTRACT

This study investigates pulsation phenomena for dual gas-assisted annular sheet nozzles, employing air and water as working fluids. Three nozzle configurations with varying liquid sheet thickness were examined experimentally utilizing high-speed imaging of the primary sheet breakup, complemented by CFD analyses to clarify the underlying physical mechanism for the observed pulsation. Numerical results revealed that the pulsation originates from liquid-sheet pinching induced by the outer gas stream, causing pressure buildup within the central gas flow and subsequent radial expansion of the liquid sheet.

Experimental results obtained over a broad range of operating conditions show that increasing either inner or outer gas velocity, or liquid velocity, generally increases the pulsation frequency, whereas increasing liquid sheet thickness leads to a decrease. Based on the experimental data, an empirical correlation for calculation of the pulsation frequency as a function of the major operating parameters was proposed. However, the pulsation frequency is primarily governed by liquid sheet thickness and liquid velocity.

1. Introduction

Gas-assisted atomization processes are utilized in numerous industrial applications, including spray drying, coating, gas cleaning, combustion and synthesis processes. Among the various atomizer concepts, dual gas-assisted annular sheet nozzles are particularly promising in terms of minimizing droplet size for high throughput (Ibrahim and Jog, 2008; Wahono et al., 2008; Wachter et al., 2021). These nozzles discharge the liquid through an annular slit as a sheet, which is subsequently disintegrated by two separate gas flows: one supplied through a central circular tube and the other through an annular channel surrounding the liquid sheet. Despite their broad relevance, the influence of process conditions and nozzle geometry on primary breakup is still not fully understood. The presence of two independently supplied gas streams introduces additional interfacial shear layers and interaction mechanisms, resulting in a more complex conversion of the liquid sheet into droplets compared to gas-assisted atomization driven by a single gas stream.

The disintegration of liquid sheets is typically initiated by the formation of surface waves, leading to an oscillating or pulsating spray pattern. This observation has been repeatedly reported in the literature, e.g., Dombrowski and Fraser (1954) and Stapper and Samuelsen (1990) for planar sheets and Kendall (1986) and Strasser et al. (2026) for circular annular sheets atomized solely by an inner gas jet (twin-fluid annular sheet nozzles). Similar pulsation patterns were observed by Richter et al. (2026) in investigations of the primary breakup of dual gas-assisted annular sheet nozzles.

The primary breakup, which describes the initial disintegration of the compact liquid flow, governs the resulting spray characteristics — both in the near-nozzle region and throughout the subsequent spray development. Consequently, a detailed understanding of the atomization process — and in particular the pulsation dynamics of liquid sheets — is important to optimize atomization performance. The present study aims to provide a time-resolved physical description of pulsation dynamics in dual gas-assisted annular sheet nozzles, to quantify the influence of operating conditions and nozzle geometry on pulsation frequency, and to derive an empirical correlation for predicting pulsation frequency. These findings contribute to a more comprehensive understanding of liquid sheet disintegration and spray formation.

Theoretical and experimental studies of the atomization of liquids investigating dual gas-assisted sheet nozzles are limited. The primary breakup of liquid sheets subjected to two gas flows was studied experimentally by Chatterjee et al. (2015) through high-speed imaging,

* Corresponding author.
E-mail address: juliana.richter@kit.edu (J. Richter).
URL: https://www.itc.kit.edu/english/390.php (J. Richter).

https://doi.org/10.1016/j.ijmultiphaseflow.2026.105969
Received 24 April 2026; Received in revised form 22 September 2026; Accepted 17 October 2026
Available online 28 October 2026
0301-9322/© 2026 The Authors. Published by Elsevier Ltd. This is an open access article under the CC BY license (http://creativecommons.org/licenses/by/4.0/).
Open access funding enabled and organized by Projekt DEAL.

Nomenclature

Latin symbols

$A_{g,i}$, $A_{g,o}$	Inner, outer gas orifice area (m^2)
a	Scaling factor (–)
$d_{g,i}$	Diameter of the central tube (m)
f	Pulsation frequency (s^{-1})
$\dot{J}_{g,i}$, $\dot{J}_{g,o}$	Inner, outer gas momentum flow rate (N)
$M_{g,struc}$	Mass of gas enclosed (kg)
$\dot{M}_{g,i}$, $\dot{M}_{g,o}$	Inner, outer gas mass flow rate (kg s^{-1})
$\dot{M}_l$	Liquid mass flow rate (kg s^{-1})
$p_{dyn,g,o}$	Dynamic pressure of the outer gas stream (Pa)
$p_{stat,struc}$	Static pressure of the gas-filled structure (Pa)
R	Specific gas constant (J (kg K)$^{-1}$)
$s_{g,o}$	Thickness of outer annular slit (m)
s_l	Liquid sheet thickness (m)
T	Temperature (K)
t	Time (s)
$v_{g,i}$, $v_{g,o}$	Inner, outer gas velocity (m s^{-1})
v_l	Liquid velocity (m s^{-1})
v_p	Propagation velocity (m s^{-1})
V_{struc}	Volume of the gas-filled structure (m^3)

Greek symbols

α	Liquid volume fraction (–)
α_{s_l}	Damping coefficient (m^{-1})
$\beta_{g,i}$, $\beta_{g,o}$, β_l	Velocity exponents (–)
δ_w	Nozzle wall thickness (m)
λ	Axial distance (m)
$\rho_{g,i}$, $\rho_{g,o}$	Density of inner, outer gas stream (kg m^{-3})

leading to the identification of five distinct breakup modes for kerosene sheets, most of which have not been reported in other studies. These include: (i) *jet mode*, in which the liquid sheet issues as a continuous jet without significant disintegration, (ii) *necklace mode*, which is characterized by a droplet chain-like structure, (iii) *early breakup mode*, which features complete sheet disintegration in the near-nozzle region and is conceptually analogous to the prompt atomization described by Lefebvre (1992), (iv) *onion-type mode*, where the liquid bulges outward before re-converging in the axial direction, and (v) *perforated conical sheet mode*, marked by the formation of holes within the expanding conical liquid sheet. Based on these findings, Richter et al. (2026) systematically investigated the influence of inner gas, outer gas, and liquid flow as well as liquid sheet thickness. They classified breakup modes into the two main categories: **bubble-induced**, as will be illustrated and discussed in more detail in the context of Fig. 8, and **non-bubble-induced**. **Bubble-induced** modes — such as *Rayleigh* (first described by Kendall (1986) and Choi and Lee (1997) for twin-fluid sheet nozzles), *inner/outer gas-driven bubble breakup*, *pure pulsating* (first reported by Choi and Lee (1997) for twin-fluid sheet nozzles), *Christmas tree* (introduced by Adzic et al. (2001) for dual gas-assisted sheet nozzles), *pulsating atomization* and *membrane-dominated mode* — are initiated by bubble formation and bursting, and display a periodic, radial expansion of the liquid sheet, resulting in a pulsating spray pattern. The findings of Leboucher et al. (2010) further support the existence of **bubble-induced** breakup modes, as they also observed the *Rayleigh mode*, the *bubble breakup* and the *Christmas tree regime*. Richter et al. (2026) further identified the *pulsating atomization mode* — characterized by a pronounced radial expansion of the liquid sheet — as the regime most commonly observed under a wide range of operating conditions. **Non-bubble-induced** modes include *beads-on-a-string*, *membrane-like breakup* (described by Chigier and Faragó (1992) for jet nozzles), *fiber type breakup* (also described by Chigier and Faragó (1992) for jet nozzles) and *prompt atomization mode* (originally introduced by Lefebvre (1992) for jet nozzles).

Table 1
Nozzle data (Nozzle 1–3).

	$d_{g,i}$ in mm	s_l in mm	$s_{g,o}$ in mm
Nozzle 1	3	1	4.1
Nozzle 2	3	2	3.6
Nozzle 3	3	3	3.1

Theoretical studies of dual gas-assisted annular sheet nozzles — hereafter referred to as sheet nozzles — complement experimental observations by describing surface instabilities that drive sheet breakup. Linear and nonlinear stability analyses revealed that both sheet surfaces oscillate either nearly in phase (with a phase shift close to zero) or nearly out of phase (with a phase shift close to π), resulting in para-sinuous and para-varicose wave modes, respectively Ibrahim and Jog (2008), Shen and Li (1996), Cao (2005) and Duke et al. (2012). Unlike strictly sinuous or varicose waves, which correspond to precisely defined phase shifts of 0 or π, the prefix para — denotes wave modes with phase shifts close to these values. Para-sinuous surface waves exhibit higher growth rates than para-varicose modes, and growth rates increase with liquid sheet thickness as well as with relative and absolute gas velocities. High-speed imaging by Wahono et al. (2008) confirmed that sheet rupture is dominated by sinuous waves, corresponding to strictly in-phase oscillations (phase shift $\approx$ 0), rather than the para-sinuous modes described in theoretical analyses. The periodic radial expansion of the liquid sheet and subsequent breakup into ligaments and large droplets observed in **bubble-induced** modes may be regarded as a macroscopic manifestation of these underlying surface waves.

Computational studies (CFD) applying volume-of-fluid methods have further classified pulsation phenomena in internal-mixing sheet nozzles, where inner gas and liquid interact inside the nozzle, with respect to their appearances and frequencies (Strasser, 2011). Where feasible, CFD predictions were validated against high-speed imaging data. In a subsequent study, Strasser and Battaglia (2017b) examined the influence of nozzle geometry — particularly contrasting internal and external mixing configurations, in which gas and liquid interact only outside the nozzle — on the evolution of pulsation pattern. The external mixing design was found to promote a stronger lateral dispersion of the pulsation-induced ligaments and large droplets at low inner gas flow. This observation is consistent with the larger droplet sizes reported for external mixing nozzles by Strasser and Battaglia (2018). In summary, previous studies have established the existence of pulsating breakup modes in dual gas-assisted annular sheet nozzles. However, comprehensive experimental data quantifying the influence of inner gas flow, outer gas flow, liquid flow and liquid sheet thickness on pulsation frequency across a broad operating range remain limited for external mixing dual gas-assisted annular sheet nozzles. To address this gap, the present study conducts a systematic experimental investigation focused exclusively on pulsation phenomena in annular liquid sheets. The experiments were designed to isolate the influence of key operating parameters and nozzle geometry, thereby providing direct insights into the dependence of pulsation characteristics on liquid sheet thickness, inner and outer gas flow and liquid flow. Three sheet nozzles with varying liquid sheet thicknesses (s_l) were utilized. The inner gas orifice areas ($A_{g,i}$) were kept constant. The outer gas orifice areas ($A_{g,o}$) were maintained approximately constant by adjusting the outer gas gap widths ($s_{g,o}$); deviations remained within 2.2%, dictated by manufacturing tolerances. Accompanying CFD-simulations were performed, offering access to physical quantities not measurable in experiments and enabling a physical interpretation of the observed pulsations.

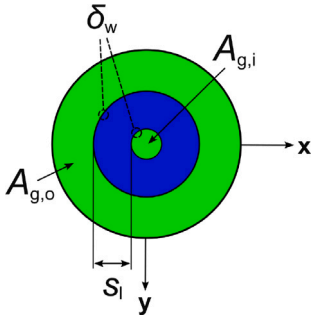


Fig. 1. Nozzle top view. (For interpretation of the references to color in this figure legend, the reader is referred to the web version of this article.)

2. Setup

2.1. Experimental setup

As described in detail by Sänger (2018), the experimental setup consists of the atmospheric spray test rig (ATMO) in combination with a high-speed camera (HSC). A schematic of the spray test rig ATMO is shown in Fig. 2(i). Sheet nozzles are mounted on an axially movable (z-direction) three-fluid lance. The liquid mass flow, supplied by an eccentric screw pump, was controlled in the range of $\dot{M}_l = 5$–100 kg h^{-1} and measured with a Coriolis flow meter (Bronkhorst High-Tech B.V.) with an uncertainty of 0.1%. Compressed air was supplied through two separate lines with hot-wire anemometers and precision control valves (Bronkhorst High-Tech B.V., uncertainty 0.1%), enabling mass flow rates of 0.4–20 kg h^{-1} (inner) and 10–100 kg h^{-1} (outer). A honeycomb flow straightener was installed at the inlet of the spray collection tank to suppress droplet recirculation.

Three external-mixing sheet nozzles were employed to atomize water with pressurized air (see Table 1). A schematic of the cross-sectional view of the utilized nozzles is shown in Fig. 2(ii). The liquid (blue) was discharged through an annular slit with thickness s_l, which was varied in the steps of 1, 2 and 3 mm. Surrounding the liquid sheet, two coaxial gas flows (green) were introduced: the inner gas through a circular central tube with diameter $d_{g,i}$ and the outer gas through an annular slit (Fig. 1) with thickness $s_{g,o}$. Keeping both the inner and outer gas orifice areas constant across all nozzles applied ensured that, for any given inner and outer gas velocity, the resulting gas momentum flows were identical for all nozzle configurations. This approach allows for the isolated investigation of the effect of liquid sheet thickness on the pulsation phenomenon. The walls of the tubes separating liquid and gas at the nozzle exit have a thickness of $\delta_w = 0.1$ mm in order to minimize coaxial gas flow disturbance by Tian et al. (2014), see Fig. 1. Although the authors focused on the atomization of liquid jets rather than annular liquid sheets, no significant influence of wall thickness was observed for a nozzle geometry with dimensions comparable to the smallest liquid sheet investigated in the present study (jet diameter of 0.97 mm, wall thickness of 0.15 mm). Therefore, the effect of wall thickness is expected to be negligible. Liquid sheet breakup was recorded using a high-speed camera HSC (Phantom v1840, Vision Research) in two configurations: HSC1 and HSC2. An overview of both settings is provided in Table 2. The corresponding fields of view are indicated in Fig. 2(ii). Backlight illumination was realized with a high-intensity LED array (LED 4438-Boost, High Speed Vision GmbH, peak power 1000 W). The strong illumination enabled extremely short exposure times of 1 and 1.5 µs, ensuring sharp images of the rapid disintegration process. For each operating condition, at least 1000 high-speed images were acquired, along with a background reference image recorded without liquid flow.

Table 2
High-speed camera settings.

Setting	HSC1	HSC2
Resolution in px	1280 × 800	2048 × 1952
Field of view in mm^2	36 × 22	76 × 73
z position in mm	0	
Focal length in mm	105	
Frame rate in Hz	4500	
Aperture	5.6	8
ISO	4000	3200
Shutter speed in µs	1	1.5

2.2. Numerical setup

The experimental study is complemented by numerical analyses conducted for selected operating conditions. We note that the motivation for the numerical study in the present work is to accompany the experimental analysis and to provide additional information helping to explain the experimentally-observed pulsation phenomenon, see Section 3.1. A detailed CFD analysis of the full experimental series is beyond the scope of the present paper and the subject of future work. To our best knowledge, only Strasser and Battaglia (2017b) have conducted combined numerical and experimental investigations of external-mixing annular sheet nozzles in the past. Their numerical approach was based on RANS and used either axi-symmetric 2D setups or 3D wedge domains. In Strasser and Battaglia (2017a) the same authors showed that fundamentally different RANS models like RSM and SST can predict essentially the same flow physics.

The present study employs a large eddy simulation (LES) approach. Since the LES paradigm requires the resolution of the large, energy-containing turbulent structures and turbulence is inherently three-dimensional (3D), a full 360° 3D domain is employed to capture (the high kinetic energy part of) the vortex stretching mechanism present in all turbulent flows (Pope, 2000). We use the volume of fluid (VOF) method available in the open-source C++ library OpenFOAM (OpenFOAM, 2023), which applies the PIMPLE algorithm for pressure-momentum coupling. The VOF method and its implementation of interface compression in the transport equation of the liquid volume fraction α in OpenFOAM (Cifani et al., 2016, Eq. (30) therein and subsequent closure eqns.) have been extensively described in Cifani et al. (2016), Deshpande et al. (2012) and are only referenced here. The surface tension model uses the continuum surface force (CSF) approach proposed by Brackbill et al. (1992). Unresolved contributions by the convective term of the momentum equation are closed by the eddy viscosity assumption, as described in Saeedipour and Schneiderbauer (2021) using the Wall-Adapting Local Eddy Viscosity model by Nicoud and Ducros (1999).

The computational domain and mesh are based on nozzle 3 described in Table 1 and shown in Fig. 3. The domain extends upstream into the nozzle to allow the flow to develop from its imposed inlet condition set as a uniform velocity profile corresponding to the experimental mass flow rate. Simulations with different upstream configurations confirmed that these flow diversions do not alter the large-scale breakup dynamics or the pulsation frequency of the primary breakup. The computational grid consists of 9.5 million hexahedral cells, resolving $\Delta_z = 100$ µm and $\Delta_r = 50$ µm within the densest regions, i.e. the shear layers and the inflow channels. Following the guideline proposed by Pope in Pope (2000), the resolved turbulent kinetic energy was kept at 80 percent and above in the region of interest and only fell slightly below 80% in coarser areas remote from the breakup region. The grid sufficiently captures the large-scale event of the primary breakup close to the nozzle exit, whereas resolving the further disintegration of the ligaments is beyond the scope of this study. No-slip boundary conditions are applied at all walls. The near-wall region (on average $2 < y^+ < 6$) is treated using a wall-modeled LES approach, employing a

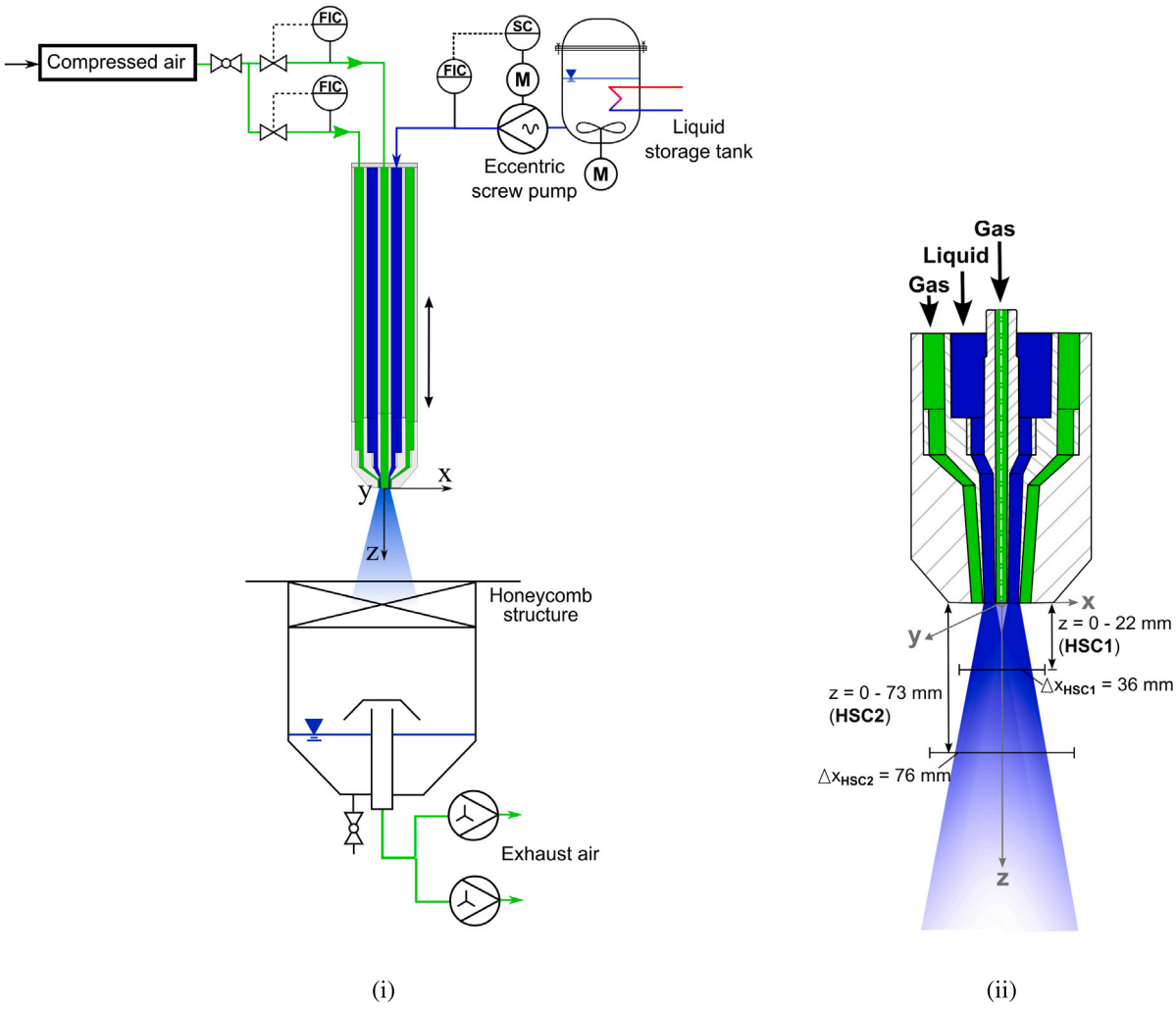


Fig. 2. Schematic of the experimental setup: atmospheric spray test rig (ATMO) (i); nozzle cross-sectional view (ii). (For interpretation of the references to color in this figure legend, the reader is referred to the web version of this article.)

wall function based on Spalding's law (Spalding, 1961) for the subgrid-scale viscosity. The pressure at the walls and at the gas and water inlets is adjusted to ensure consistency with the imposed velocity field. At the outlets, the pressure is set to 1 bar absolute, while the velocity is treated with a pressure-driven open boundary condition allowing for outflow and possible entrainment. Numerical schemes are adapted from our previous studies on twin-fluid jet atomizers (Zhang et al., 2023). Transient terms are discretized using a first-order implicit Euler scheme required for computational stability, similar to Sun et al. (2025). Spatial discretization is performed using second-order finite volume schemes for the convective terms (Zhang et al., 2020). The timestep is adapted to a maximum Courant number of 0.5. However, the Courant number of cells at the interface is kept strictly below 0.2 (Roenby et al., 2016) and four corrector loops for the advection of the liquid volume fraction are employed. Statistical sampling started after a flow initialization period of 20 gas flow-through times, which corresponds to a physical time of $t = 0.02$ s. Sampling was conducted for a period of 20 ligament traversal times, which corresponds to a physical time of $\Delta t = 0.23$ s, resulting in more than 1000 samples for meaningful statistics.

3. Results and discussion

The experimental investigation comprises three test series addressing (a) the influence of inner and outer gas velocity, (b) the effect of liquid sheet thickness, and (c) the impact of the liquid mass flow rate. Complementary numerical simulations were performed at a representative operating point specified as (for definitions of Re and Ma see below):

- $s_l = 3$ mm,
- $\dot{M}_{g,i} = 2$ kg h^{-1} ($Re_{g,i} = 13{,}000$), $Ma_{g,i} = 0.19$,
- $\dot{M}_l = 60$ kg h^{-1} ($Re_l = 1800$),
- $\dot{M}_{g,o} = 24$ kg h^{-1} ($Re_{g,o} = 18{,}600$), $Ma_{g,o} = 0.13$

The complete set of operating conditions is summarized in Table 3, with sheet thickness (s), mass flow rate ($\dot{M}$) and velocity (v). The subscripts "l", "g,i" and "g,o" indicate liquid, inner and outer gas. The corresponding dimensionless numbers, including Reynolds (Re), aerodynamic Weber (We_{aero}) and Mach (Ma) numbers, are listed in Table 4. The dimensionless numbers are defined as

$$Re_j = \frac{v_j \cdot \rho_j \cdot L_{c,j}}{\eta_j} \tag{1}$$

$$We_{aero,j} = \frac{(v_j - v_l)^2 \cdot \rho_j \cdot 2s_l}{\sigma} \tag{2}$$

$$Ma_j = \frac{v_j}{c} \tag{3}$$

where ρ denotes density, η dynamic viscosity, σ surface tension, c speed of sound and L_c characteristic length. For the calculation of the dimensionless numbers, the characteristic length is defined as $2s_l$ for

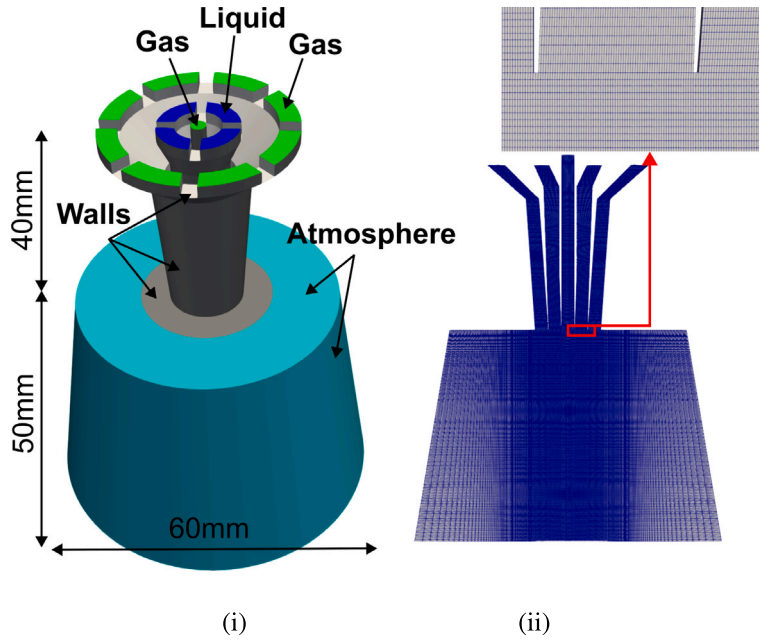


Fig. 3. Numerical setup. (i) Computational domain and boundary conditions, (ii) Cross-sectional view of the mesh with a zoom into the liquid filled inlet region.

Table 3
Operating conditions of the experiments.

	s_l in mm	$\dot{M}_{g,i}$ in kg h^{-1}	$v_{g,i}$ in m s^{-1}	$\dot{M}_l$ in kg h^{-1}	v_l in m s^{-1}	$\dot{M}_{g,o}$ in kg h^{-1}	$v_{g,o}$ in m s^{-1}
(a)	1	0.4–1.4	13–46	60	1.3	5–15	9–28
(b)	1/2/3	2	65	60	1.3/0.5/0.3	24–72	45–137
(c)	1/2/3	2	65	5–100	0.21/0.36/0.48	68	130

the liquid sheet, $d_{g,i}$ for the inner gas flow, and $2s_{g,o}$ for the outer gas flow (see Table 1).

3.1. Physical description of the pulsation phenomena

In the following, a pulse refers to a single atomization event characterized by the radial expansion of the liquid sheet and its subsequent breakup into ligaments and droplets, whereas pulsation refers to the associated periodic process comprising a sequence of such pulses. Fig. 4 compares experimental observations with numerical predictions, indicated by an iso-contour of the liquid volume fraction $\alpha = 0.3$. The absence of visible liquid further downstream in the simulation is due to the decreasing ligament size relative to the increasing cell size, causing the ligaments to fall below the threshold of the iso-contour used for illustration purposes. t is the absolute time normalized by the characteristic frequency $f = 50$ s^{-1} and is held consistent with the temporal sequence in Fig. 6 which will be discussed at the end of this section.

The temporal progression of a pulse in the *pulsating atomization mode* shown in Fig. 4 is not only captured experimentally but also reproduced in the simulation. Owing to the periodic nature of the pulsation process, the pulsation frequency, captured by HSC images, was determined via a Fast Fourier Transform (FFT) analysis using the SPRAYCAT MATLAB toolbox following the methodology outlined in Sänger et al. (2016). For this purpose, the HSC images were converted into binary images using Otsu thresholding. Subsequently, a time-dependent signal was obtained from the number of dark pixels (black pixels in the resulting binary image) along a predefined evaluation line in the y-direction at a fixed axial position z. Following this, the dominant pulsation frequency was identified from the FFT spectrum of this signal. For the evaluation of the LES data, a xy-plane was placed through the domain

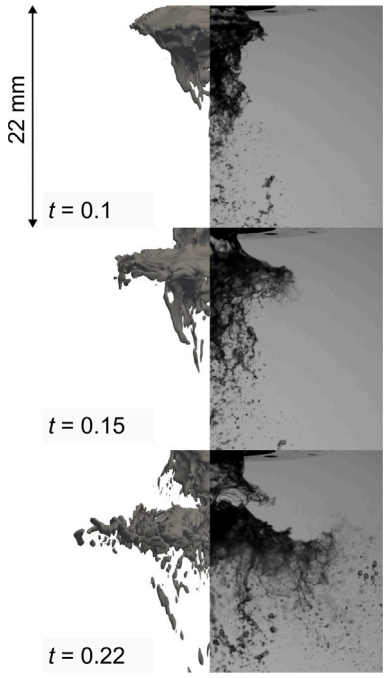


Fig. 4. Temporal sequence of a pulse for $s_l = 3$ mm, $\dot{M}_{g,i} = 2$ kg h^{-1} ($Re_{g,i} = 13{,}000$), $\dot{M}_l = 60$ kg h^{-1} ($Re_l = 1800$), $\dot{M}_{g,o} = 24$ kg h^{-1} ($Re_{g,o} = 18{,}600$); numerical simulation results (left) and HSC images (right). The times are normalized by the characteristic frequency of $f = 50$ s^{-1}.

corresponding to the z-position that was analyzed in the image post-processing of the aforementioned toolbox. In this plane, cells with a liquid volume fraction ≥0.5 were considered for post-processing along the y-axis. Each y-position was counted once if at least one such cell was present along the corresponding x-axis. This evaluation reduces the two-dimensional spray distribution to the HSC view, which captures the spray without resolving its distribution in x-direction. The resulting one-dimensional signal was then subjected to FFT analysis, ensuring methodological consistency between experiment and simulation. Fig. 5

Table 4
Dimensionless numbers corresponding to the investigated operating conditions listed in Table 3.

	$Re_{g,i}$	Re_l	$Re_{g,o}$	$We_{aero,g,i}$	$We_{aero,g,o}$	$Ma_{g,i}$	$Ma_{g,o}$
(a)	2600–9200	2500	5200–15,500	4.7–66	2.2–24.5	0.04–0.13	0.03–0.08
(b)	13,000	1800/2000/2500	18,600–74,900	136/278/419	64–1900	0.19	0.13–0.40
(c)	13,000	400–2900	62,400/53,700/71,000	139–420	560–1700	0.19	0.38

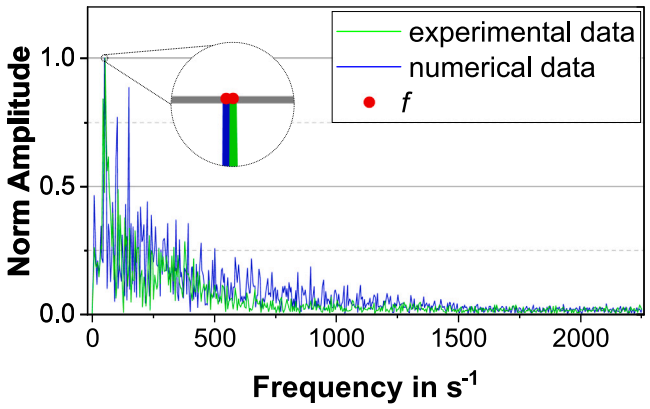


Fig. 5. Frequency analysis of the time-dependent intensity signal derived from the number of dark pixels in the spray image and number of cells with $\alpha \geq 0.5$ in the simulation at a measurement plane located at $z = 9$ mm. The resulting spectrum is normalized by the respective maximum amplitude. The spectrum exhibits a dominant component corresponding to the pulsation frequency at $f \approx 50$ s^{-1} for $s_l = 3$ mm, $\dot{M}_{g,i} = 2$ kg h^{-1} ($Re_{g,i} = 13{,}000$), $\dot{M}_l = 60$ kg h^{-1} ($Re_l = 1800$), $\dot{M}_{g,o} = 24$ kg h^{-1} ($Re_{g,o} = 18{,}600$); frequency spectra based on the HSC images (green) and numerical simulation data (blue). (For interpretation of the references to color in this figure legend, the reader is referred to the web version of this article.)

shows very good agreement of the fundamental pulsation frequency f captured in the experiments at 53 s^{-1} and in the simulation at 48 s^{-1}. This is consistent with previous RANS-based simulations (Strasser and Battaglia, 2017b), which have also demonstrated that the relevant pulsation frequencies can be captured at lower computational cost. Furthermore, these studies provided valuable insights into the flow structures within a 3D, but circumferentially reduced computational domain. The present LES extends these previous findings by resolving the full 360° flow domain, thereby providing instantaneous insights into the underlying transient and asymmetric flow dynamics before and after the pulse, see Fig. 6.

The progressive constriction of the liquid sheet, which starts at the outer surface of the liquid sheet and subsequently propagates inward, causes a gradual reduction in the cross-sectional area available for the inner gas stream. This process is illustrated in Fig. 6 by the temporal evolution of the instantaneous static pressure field and the white-contoured liquid–gas interface between $t = 0.0$ to 0.04, where t is the absolute time normalized by the characteristic frequency $f = 50$ s^{-1} and defined as zero at the beginning of the pulse. This spatial confinement leads to a continuous pressure increase within the central gas core, i.e, the gas pressure rises due to the restricted flow passage. In Fig. 6, this increase is evident at $t = 0.03$ and 0.04 from the emergence of warmer color regions (yellow, red). This elevated pressure induces a radially outward inflation of the gas-filled liquid structure, as visible in Fig. 6 between $t = 0.05$ and $t = 0.09$ and consistent with the observations reported by Richter et al. (2026). A rupture event of this structure occurs between $t = 0.09$ and $t = 0.13$. Such rupture may occur via two different mechanisms: Either the liquid sheet becomes progressively thinner during the inflation until it loses its structural integrity, or externally imposed aerodynamic forces exceed the stabilizing capillary and viscous forces of the liquid, causing it to rupture. The rupture event marks the end of a pulse, but not necessarily the beginning of the next one. The time between two subsequent pulses is a function of operating conditions. This interpretation of pulse formation as a process driven by increasing pressure and subsequent rupture is supported by the dominant frequency obtained from the simulated pressure signal (48 s^{-1}), which is in good agreement with the dominant pulsation frequency identified in Fig. 5.

A pressure build-up and subsequent relief mechanism has also been reported previously for internal mixing annular sheet nozzles by Strasser and Battaglia (2016). In that configuration, the pressure increase was associated with liquid bridging and fountain formation inside the nozzle. In contrast, the present external mixing nozzle configuration exhibits a transient constriction of the inner gas passage caused by the inward deformation of the liquid sheet in the vicinity of the nozzle exit. Although both mechanisms involve a pressure increase followed by rupture, the underlying flow configurations and the cause of the pressure rise differ.

Following the interpretation of a pulse as a macroscopic manifestation of a surface wave, the deformation of the liquid sheet in Fig. 6 exhibits a qualitatively sinusoidal nature: the inner and outer sheet interfaces move largely in parallel, both inward (e.g., at $t = 0.03$) and outward (e.g., at $t = 0.09$). While the deformation does not constitute a fully developed wave, its qualitative sinusoidal features correspond to the characteristics noted by Wahono et al. (2008) and reported by Strasser and Battaglia (2017b) for the flushed nozzle design, where the inner gas, liquid and outer gas channels terminate in the same axial plane. A schematic of the cross-sectional view of the utilized nozzles is shown in Fig. 2(ii). The operating point examined in Figs. 5 and 6 was selected as a representative case; analogous trends were also observed for other operating conditions.

3.2. Experimental investigation of the pulsation frequency

After establishing the physical mechanisms underlying pulsation in Section 3.1, the next step is to quantify its characteristics based on experimental data. In particular, pulsation frequency, defined as the repetition rate of individual pulses, is a governing parameter for characterizing and assessing pulsation phenomena. This rate is equivalent to the rupture frequency, as both the inflation and the subsequent rupture of the liquid structure belong to the same pulse. Experimental studies were conducted to assess the impact of operating parameters and liquid sheet thickness s_l on the pulsation frequency f.

3.2.1. Influence of inner and outer gas velocity on pulsation frequency

The periodic appearance of the pulsation phenomenon produces an axially repeating pattern of inflated liquid structures. Thus, the pulsation frequency can be expressed as:

$$f \propto \frac{v_p}{\lambda} \tag{4}$$

where v_p denotes the axial propagation velocity of the inflated liquid structure and λ is the axial distance between the positions of maximum radial extent of two consecutive inflated liquid structures.

The propagation velocity v_p was obtained from HSC recordings at the optically accessible outer gas–liquid interface. It was determined by tracking the axial displacement Δz at the point of maximum radial expansion, see Fig. 7, over the corresponding time interval Δt, using $v_p = \Delta z / \Delta t$.

Fig. 8 shows the breakup mode classification reported by Richter et al. (2026) for $s_l = 1$ mm and a liquid mass flow rate of $\dot{M}_l = 60$ kg

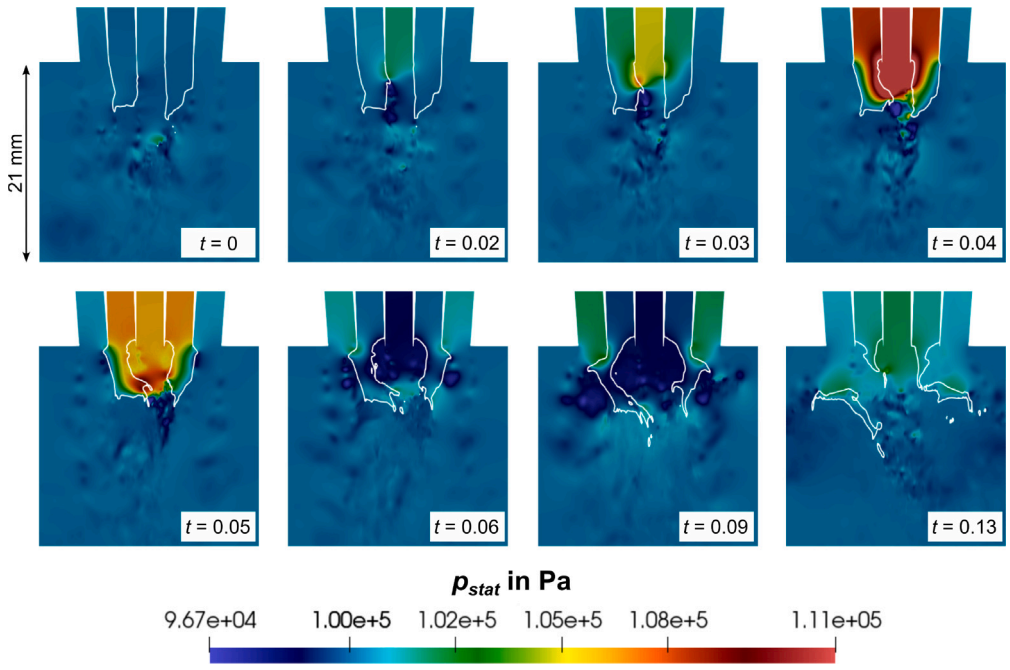


Fig. 6. Time sequence of instantaneous slices through the centerline of the computational domain showing the liquid–gas interface (white contour at $\alpha = 0.3$) superimposed on the static pressure field in Pa. The times are normalized by the characteristic frequency of $f = 50\ s^{-1}$. Operating conditions: $s_l = 3$ mm, $\dot{M}_{g,i} = 2$ kg h^{-1} ($Re_{g,i} = 13{,}000$), $\dot{M}_l = 60$ kg h^{-1} ($Re_l = 1800$), $\dot{M}_{g,o} = 24$ kg h^{-1} ($Re_{g,o} = 18{,}600$). Data derived from VOF-LES. (For interpretation of the references to color in this figure legend, the reader is referred to the web version of this article.)

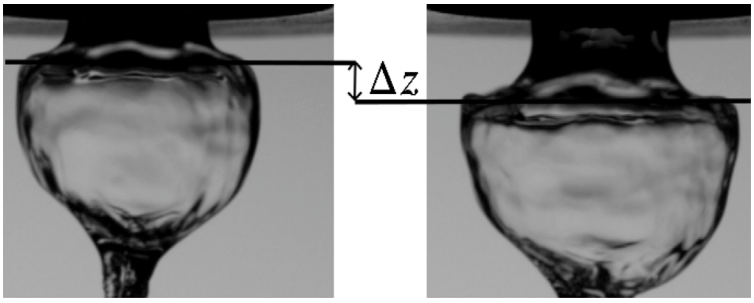


Fig. 7. HSC visualization for determination of propagation velocity v_p; t_2 (right) > t_1 (left), where t denotes time.

h^{-1}, as a function of the inner ($\dot{J}_{g,i}$) and outer gas momentum flow rates ($\dot{J}_{g,o}$), defined as

$$\dot{J}_j = v_j^2 \cdot \rho_j \cdot A_j \tag{5}$$

where A denotes the exit orifice area and the subscript j refers to the inner gas stream (g,i) or the outer gas stream (g,o). The filled symbols indicate the operating conditions examined for the investigation of v_p in this study (Table 3(a)). In the *pulsating atomization mode*, see Fig. 8 top right, liquid disintegration occurs near the nozzle orifice, precluding a reliable determination of Δz via HSC diagnostics. As the fundamental pulsation mechanism persists across all **bubble-induced** regimes, the operating conditions were systematically adjusted towards lower gas flow rates, thereby enabling the observation of additional **bubble-induced** breakup modes. In these regimes, the liquid breakup occurs at larger axial distances, allowing for an accurate determination of v_p.

Increasing the inner gas momentum flow rate from $\dot{J}_{g,i} = 0.0015$ N to 0.018 N at a constant outer gas momentum flow rate of $\dot{J}_{g,o} = 0.026$ N (corresponding to $v_{g,o} = 13$ m s^{-1}) leads the breakup mode to evolve from the *Rayleigh mode* to the *inner gas-driven bubble mode* and finally to the *pure pulsating mode*. Conversely, maintaining the inner gas momentum flow rate at $\dot{J}_{g,i} = 0.0015$ N (corresponding to $v_{g,i} = 13$ m s^{-1}) and increasing the outer gas momentum flow rate from $\dot{J}_{g,o} = 0.013$ N to 0.12 N causes the breakup to evolve from the *Rayleigh mode* to the *outer gas-driven bubble breakup mode* and finally to the *Christmas tree mode*. Despite their different appearances (see Fig. 8), all of these modes are classified as **bubble-induced**, characterized by a periodic formation and disintegration of gas-filled liquid structures.

As the pulsation frequency f depends on both the propagation velocity v_p and the axial distance λ (Eq. (4)), a qualitative consideration of λ is required. Fig. 8 therefore includes schematic illustrations of λ for the *inner* and *outer gas-driven bubble breakup mode*. An increase in $v_{g,i}$ is associated with a reduced λ; whereas, a higher $v_{g,o}$ results in a larger λ, consistent with the characteristic differences in appearance observed between these breakup modes.

Fig. 9 presents the propagation velocities v_p (top) and pulsation frequencies f (bottom) as functions of the inner and outer gas velocity. In both diagrams, filled symbols refer to cases with constant $v_{g,i}$ (varying $v_{g,o}$), whereas hollow symbols correspond to constant $v_{g,o}$ (varying $v_{g,i}$).

In Fig. 9 (top), v_p increases almost linearly with gas velocity in both cases, with a more pronounced increase when the outer gas velocity is varied. This stronger increase with $v_{g,o}$ is attributed to the outer gas interacting axially with a larger surface area of the gas-filled liquid structure.

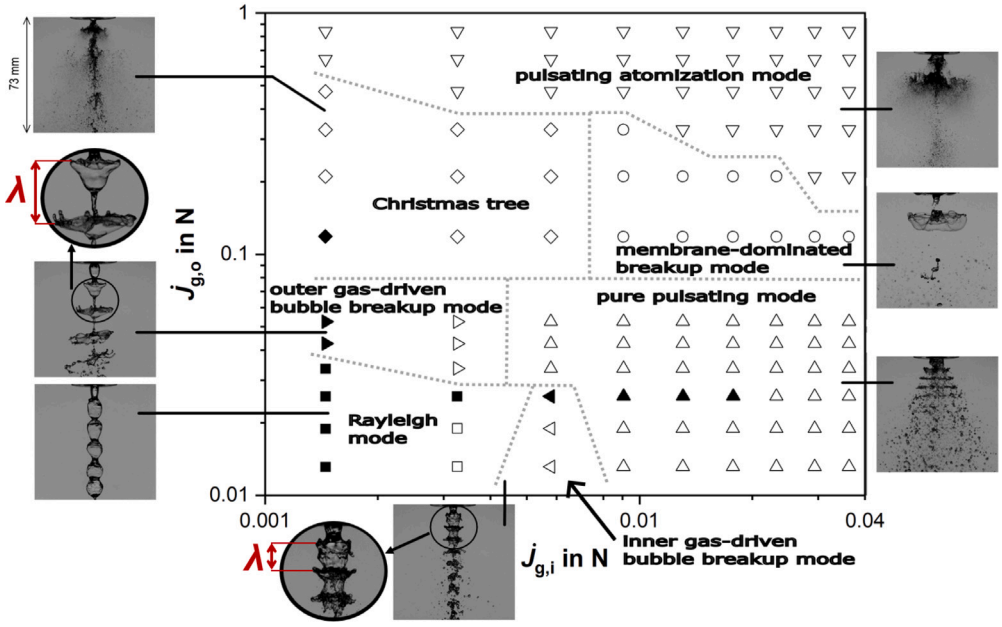


Fig. 8. Breakup mode classification based on HSC images for s_l = 1 mm, shown as function of inner and outer gas momentum flow rate ($\dot{J}_{g,i}$ and $\dot{J}_{g,o}$) at a liquid mass flow rate of $\dot{M}_l$ = 60 kg h^{-1} (Re_l = 2500), $Re_{g,i}$ = 2600–13,000, $Re_{g,o}$ = 5200–41,400, $Ma_{g,i}$ = 0.04–0.19, $Ma_{g,o}$ = 0.03–0.22.
Source: Figure adapted from Richter et al. (2026); filled symbols denote the operating range investigated in the present study.

Fig. 9 (bottom) shows that f increases with $v_{g,o}$. Two mechanisms account for this trend: First, the outer gas stream initiates a pulse by imposing an inward deformation of the liquid sheet through its dynamic pressure ($p_{dyn,g,o}$):

$$p_{dyn,g,o} = \frac{1}{2}\rho_{g,o} \cdot v_{g,o}^2 \tag{6}$$

with $\rho_{g,o}$ being the density of the outer gas stream. Increasing $v_{g,o}$ therefore intensifies the deformation, which triggers the subsequent radial inflation of the gas-filled structure, and increases f. Second, the stronger dependence of v_p on $v_{g,o}$ (Fig. 9, top) exceeds the accompanying increase in λ. Thus, the ratio v_p/λ increases with $v_{g,o}$, and f rises accordingly, consistent with Eq. (4). It should be noted that v_p determined from HSC recordings represents the initial propagation velocity of the gas-filled liquid structure in the vicinity of the nozzle exit, before subsequent gas–liquid interactions along the flow direction further affect its axial velocity. Therefore, the relation in Eq. (4) is considered in the near-nozzle region, where the gas-filled structures are formed.

In contrast, increasing $v_{g,i}$ reduces λ (HSC images in Fig. 8). This trend can be attributed to the response of the inner gas stream to the inward deformation of the liquid sheet imposed by the outer gas stream. The deformation constricts the cross-sectional area available to the inner gas flow, thereby generating an increase in static pressure, which in turn drives the subsequent radial inflation of the gas-filled structure. If the inner gas is assumed to behave ideally and to provide a qualitative estimate of the expected trends, applying the product rule to the time derivative of the ideal gas relation $p_{stat,struc} = M_{g,struc}RT/V_{struc}$ yields

$$\frac{\partial p_{stat,struc}}{\partial t} = \frac{R \cdot T}{V_{struc}} \cdot \frac{\partial M_{g,struc}}{\partial t} - \frac{p_{stat,struc}}{V_{struc}} \cdot \frac{\partial V_{struc}}{\partial t} \tag{7}$$

with $p_{stat,struc}$ as static pressure in the gas-filled liquid structure, V_{struc} as its volume, $M_{g,struc}$ as mass of the enclosed gas and R as the specific gas constant. For a given constriction rate ($\partial_t V_{struc} < 0$), $\partial_t p_{stat,struc}$ tends to increase with $\partial_t M_{g,struc}$. The latter is influenced, among other factors, by $\dot{M}_{g,i}$ (and thus by $v_{g,i}$), as the gas-filled structure is supplied by the inner gas flow. Since $\dot{M}_{g,i} = \rho_{g,i}v_{g,i}A_{g,i}$ and the inner gas nozzle exit area $A_{g,i}$ is constant, an increase in $v_{g,i}$ leads to an increase in $\dot{M}_{g,i}$ and, therefore, in the rate at which gas is supplied to and accumulates within the structure. As a consequence, the gas-filled structure ruptures closer to the nozzle, thereby shortening λ. In accordance with Eq. (4), the combined effect of increasing v_p and decreasing λ yields an increase in f with increasing $v_{g,i}$ (Fig. 9, bottom). Overall, $v_{g,o}$ both enforces constriction and increases v_p, whereas $v_{g,i}$ primarily accelerates the increase in static pressure after the onset of constriction, while its influence on v_p remains comparatively weaker. Therefore, $v_{g,o}$ has a more pronounced impact on f (Fig. 9, bottom). Similar trends have previously been reported for primary instabilities in twin-fluid jet nozzles (Sänger et al., 2016, 2014), where increasing aerodynamic forces resulted in higher instability frequencies, although the underlying instability mechanisms differ from the pulsation phenomenon investigated here.

All operating points examined in the following, see Table 3(b) and (c), lead to the *pulsation atomization mode*.

3.2.2. Influence of liquid sheet thickness on pulsation frequency

Having established the influence of the inner and outer gas stream, the subsequent investigation focuses on the effect of liquid sheet thickness s_l under varying outer gas velocities $v_{g,o}$ (Table 3(b)). This approach is motivated by previous findings documented in Wachter et al. (2021) and Zhao et al. (2018), which identified $v_{g,o}$ — in contrast to $v_{g,i}$ — as the dominant factor for droplet size.

Fig. 10 illustrates the dependence of pulsation frequency f on s_l for different $v_{g,o}$, revealing a significant influence. A pronounced decrease in f is observed with increasing s_l at constant gas velocities, and thus constant gas momentum flows. Furthermore, the influence of $v_{g,o}$ diminishes with increasing sheet thickness. For s_l = 1 mm, the frequency increases with increasing $v_{g,o}$, as also shown in Fig. 9 (bottom). Further investigations applying s_l = 2 mm and 3 mm lead to a slight decrease.

A possible explanation for the observed influence of s_l on f is the following: Fig. 6 shows that pulsation is triggered by a pressure rise in the inner gas channel, resulting from a constriction. This constriction is primarily induced by the outer gas stream, which pushes the liquid sheet inward. Deflecting a thicker sheet from axial to radial direction requires stronger aerodynamic forces due to its higher inertia. Additionally, the internal gas pressure has to reach a higher level to initiate radial expansion in thicker sheets. Consequently, the timescale

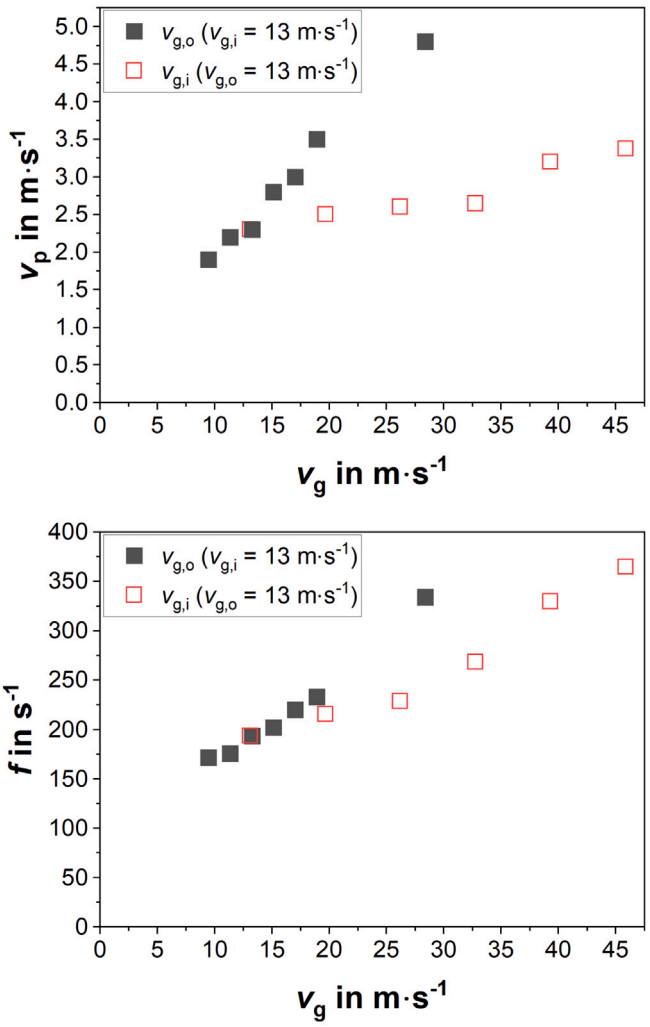


Fig. 9. Top: Propagation velocity v_p as a function of the gas velocity v_g. Bottom: Pulsation frequency f versus v_g. The experiments were conducted using the nozzle with s_l = 1 mm and a constant liquid mass flow rate of $\dot{M}_l$ = 60 kg h^{-1} (v_l = 1.3 m s^{-1}, Re_l = 2500). Data obtained from experiments.

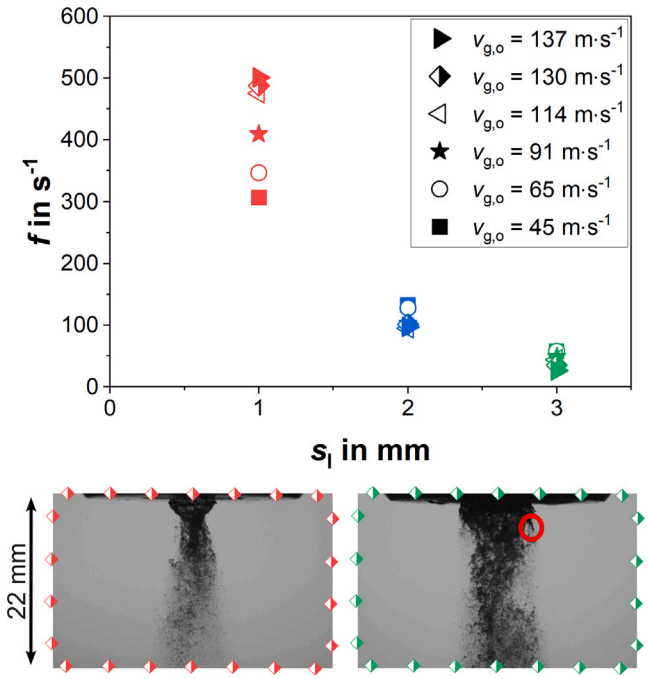


Fig. 10. Top: Pulsation frequency as a function of s_l. Bottom: HSC images of the primary sheet breakup for $v_{g,o}$ = 130 m s^{-1}, s_l = 1 mm (left, $Re_{g,o}$ = 71,000), s_l = 3 mm (right, $Re_{g,o}$ = 53,700); $\dot{M}_l$ = 60 kg h^{-1} (Re_l = 1800/2000/2500) and $v_{g,i}$ = 65 m s^{-1} ($Re_{g,i}$ = 13,000) for all cases. Data obtained from experiments. (For interpretation of the references to color in this figure legend, the reader is referred to the web version of this article.)

of pulsation formation increases with sheet thickness, leading to a lower frequency. The observed reduction in frequency is further affected by the decrease in liquid velocity v_l at constant mass flow rate with increasing sheet thickness. If two fluids flow with different velocities, a hydrodynamic instability known as a Kelvin–Helmholtz wave can form at their interface. The wave provides locations at which an inward deformation of the liquid sheet can be initiated by the outer gas stream. Previous studies by Bernal and Roshko (1986) as well as Dimotakis (1986) have shown that the convection velocity of Kelvin–Helmholtz waves increases with the liquid velocity, and that the wave frequency is proportional to the convection velocity. Consequently, a reduction in v_l lowers the rate at which such locations occur. As a result, inward deformations of the liquid sheet are initiated less frequently, which contributes to a further reduction in f. In addition, the reduction in liquid velocity increases the gas–liquid interaction time and enhances the interfacial shear. Both effects promote premature rupture before radial swelling can fully develop. These mechanisms contribute to the observed decrease in pulsation frequency with increasing $v_{g,o}$ for thicker liquid sheets. HSC images in Fig. 10 (bottom) support this interpretation. For s_l = 1 mm, the liquid sheet remains intact during radial expansion close to the nozzle exit, whereas at s_l = 3 mm, fiber-like structures detach from the sheet, initiating disintegration from the outside (highlighted exemplarily by the red circle in the right image). These observations confirm that breakup can occur prior to significant radial swelling. This effect becomes dominant with increasing sheet thickness. Therefore, we expect that a further increase in s_l beyond 3 mm will lead to an even greater suppression of pulsation events.

The HSC images in Fig. 10 (bottom) were selected to show the onset of radial expansion near the nozzle orifice and do not reflect pulsation frequency. Although the spray appears wider for s_l = 3 mm, under the given operating conditions, the s_l = 1 mm sheet produces a wider spray on average. This highlights the strong influence of pulsation dynamics: A higher pulsation frequency, corresponding to a more frequent occurrence of individual pulses, leads to broader lateral dispersion, whereas lower f result in extended non-pulsating phases that produce a narrower spray. Consequently, high frequencies promote a more homogeneous spray, while low frequencies give rise to localized droplet clouds with larger droplets and a more inhomogeneous droplet size distribution. These findings emphasize that, beyond the influence of sheet thickness on droplet size, pulsation frequency is a significant factor affecting the droplet size distribution and overall spray uniformity.

3.2.3. *Influence of liquid mass flow on pulsation frequency*

In the previous experiments, the liquid mass flow rate was kept constant. In the following, it is varied to investigate its effect on pulsation frequency (Fig. 11, Table 3(c)). The mass flow rate was increased in two distinct ways: (i) by increasing s_l at constant liquid velocity and (ii) by increasing the liquid velocity v_l at constant s_l. In the first case, the pulsation frequency decreases — consistent with the sheet thickness effect discussed earlier and shown in Fig. 10. In the second case, the frequency increases, because a higher v_l leads to a more frequent occurrence of locations at which inward deformation of the liquid sheet can be initiated. The higher liquid velocity reduces the residence time

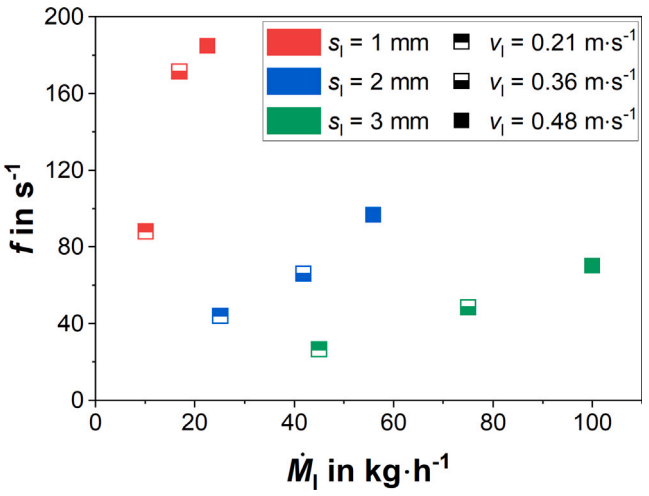


Fig. 11. Pulsation frequency as a function of $\dot{M}_l$; $v_{g,i}$ = 65 m s^{-1} ($Re_{g,i}$ = 13,000) and $v_{g,o}$ = 130 m s^{-1} ($Re_{g,o}$ = 62,400/53,700/71,000) for all cases. Data obtained from experiments.

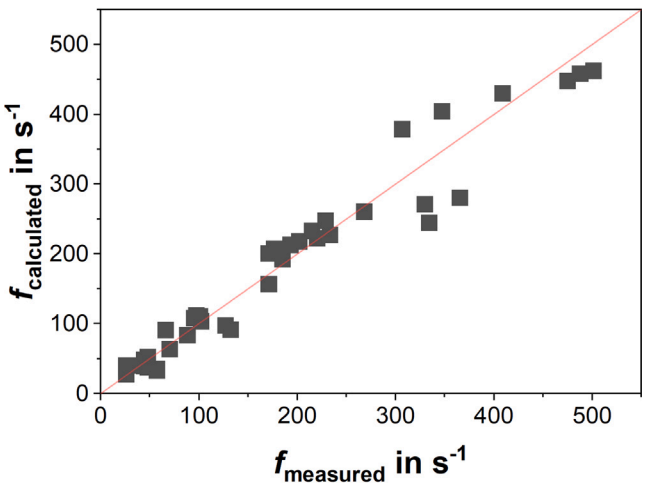


Fig. 12. Parity plot comparing the calculated pulsation frequency $f_{calculated}$ via an empirical correlation with the experimentally determined frequency $f_{measured}$.

of the liquid within the near-nozzle region, where the strongest gas–liquid interaction takes place, and decreases the interfacial shear. Both effects further contribute to this trend, consistent with the previous discussion. These findings indicate that $\dot{M}_l$ alone is not a meaningful parameter for characterizing the pulsation frequency. Instead, the underlying parameters s_l and v_l must be considered separately.

Additional dimensionless representations of the experimental data based on the Strouhal and Reynolds numbers were evaluated for the data presented in Figs. 10 and 11. However, these formulations did not provide additional physical insight. For this reason, the results are discussed in terms of the dimensional operating parameters, which allows the influence of the independently varied quantities on the pulsation frequency to be assessed more directly.

3.3. Empirical correlation for the pulsation frequency

Section 3.2 demonstrated that (i) the pulsation frequency increases with increasing inner and outer gas velocity as well as liquid velocity at fixed liquid sheet thickness, and (ii) the pulsation frequency decreases with increasing liquid sheet thickness at fixed inner and outer gas velocity, as well as liquid velocity. A central objective, therefore, is to identify which parameter exerts the strongest influence on pulsation frequency under a minimal variation.

To capture the observed trends, an empirical correlation is proposed that combines two structural components:

(i) A power-law dependence for velocity effects, discussed in Sections 3.2.1 and 3.2.3.
(ii) An exponential attenuation term for pulsation suppression, reflecting the results of Section 3.2.2.

This formulation reflects the growth of f with increasing velocities and incorporates the pronounced suppression induced by larger s_l (Eq. (8)):

$$f = a \cdot \left(\frac{v_{g,o}}{1\ \mathrm{m\ s^{-1}}}\right)^{\beta_{g,o}} \cdot \left(\frac{v_{g,i}}{1\ \mathrm{m\ s^{-1}}}\right)^{\beta_{g,i}} \cdot \left(\frac{v_l}{1\ \mathrm{m\ s^{-1}}}\right)^{\beta_l} \cdot \exp\left(-\alpha_{s_l}\frac{s_l}{1\ \mathrm{mm}}\right) \tag{8}$$

where a is a scaling factor, $\beta_{g,o}, \beta_{g,i}, \beta_l$ are velocity exponents, and α_{s_l} is a damping coefficient. All velocities $v_{g,o}$, $v_{g,i}$ and v_l are expressed in m s^{-1}, sheet thickness s_l in mm and the resulting frequency f in s^{-1}. The least-squares method yields:

$$a = 104,\ \beta_{g,o} = 0.18,\ \beta_{g,i} = 0.22, \beta_l = 0.91,\ \alpha_{s_l} = 0.55$$

with $R^2 = 0.94$, indicating good agreement with experimental data. The validity of this formulation is confirmed for the 39 sets of experimental data corresponding to the operating conditions investigated in Table 3, covering liquid mass flow rates between 5 and 100 kg h^{-1}. Fig. 12 presents a parity plot comparing the correlation-derived pulsation frequencies ($f_{calculated}$) with the experimental values ($f_{measured}$), illustrating the accuracy of the proposed empirical correlation.

Eq. (8) and the fit parameters indicate that variations in s_l have the most pronounced effect on f, followed by v_l, whereas $v_{g,i}$ and $v_{g,o}$ exert a comparatively weaker influence. Accordingly, with suitably chosen s_l and v_l, operating regions associated with low or high f can be approached, while adjustments of the gas velocities offer additional, secondary tuning.

4. Conclusion

This study presents a systematic experimental investigation focused on pulsation phenomena in annular liquid sheets, complemented by CFD simulations conducted at selected operating conditions to provide insight into the underlying physical mechanism. Three dual gas-assisted annular sheet nozzles with varying liquid sheet thicknesses were examined. High-speed visualization techniques were applied to investigate pulsation patterns. The following conclusions can be drawn:

CFD simulation — Physical mechanism of pulsation phenomenon:

1. Cause: Pinching of the liquid sheet by the outer gas stream
2. Effect: Pressure increase in the inner gas flow
3. Consequence: Radial spreading of the liquid sheet followed by rupture

Experimental observations:

1. Increasing the inner and outer gas velocity, as well as the liquid velocity, generally raises the pulsation frequency.
2. An increase in liquid sheet thickness leads to a reduction in pulsation frequency.

Empirical correlation governing pulsation frequency:

1. An empirical correlation for the pulsation frequency was formulated as a function of liquid sheet thickness, liquid velocity, and inner and outer gas velocity.

2. The correlation indicates that liquid sheet thickness has the strongest influence on the pulsation frequency, followed by liquid velocity; whereas, inner and outer gas velocities play a secondary role within the investigated parameter range.

This study provides a time-resolved physical description of the pulsation dynamics in dual gas-assisted annular sheet nozzles and suggests key parameters that govern its occurrence. Ongoing work is focused on a detailed characterization of the droplet size distribution and will be addressed in a subsequent publication to complement and extend the present findings. Future work will focus on systematic VOF-LES investigations of a broader range of operating conditions.

CRediT authorship contribution statement

Juliana Richter: Writing – review & editing, Writing – original draft, Visualization, Validation, Methodology, Formal analysis, Data curation, Conceptualization. **Julia Roeb:** Writing – review & editing, Writing – original draft, Visualization, Validation, Methodology, Formal analysis, Data curation, Conceptualization. **Tobias Jakobs:** Writing – review & editing, Supervision, Conceptualization. **Frederik Scheiff:** Supervision. **Oliver T. Stein:** Writing – review & editing, Supervision, Conceptualization. **Thomas Kolb:** Writing – review & editing, Supervision, Conceptualization.

Declaration of AI

During the preparation of this work the authors used Copilot in order to improve the language of the manuscript. After using this tool, the authors reviewed and edited the content as needed and take full responsibility for the content of the published article.

Declaration of competing interest

The authors declare that they have no known competing financial interests or personal relationships that could have appeared to influence the work reported in this paper.

Acknowledgments

The authors gratefully acknowledge the financial support by the Helmholtz Association of German Research Centres, within the research field Energy, program Materials and Technologies for the Energy Transition (MTET) (38.05.01). The authors gratefully thank Feichi Zhang for intensive and helpful discussions. The authors acknowledge support by the state of Baden-Württemberg for HPC time through bwHPC.

Data availability

Data will be made available on request.

References

Adzic, M., Carvalho, I.S., Heitor, M.V., 2001. Visualization of the disintegration of an annular liquid sheet in a coaxial airblast injector at low atomizing air velocities. Optics 5 (1), 27–38.

Bernal, L.P., Roshko, A., 1986. Streamwise vortex structure in plane mixing layers. J. Fluid Mech. 170, 499–525. http://dx.doi.org/10.1017/S002211208600099X.

Brackbill, J., Kothe, D., Zemach, C., 1992. A continuum method for modeling surface tension. J. Comput. Phys. 100 (2), 335–354. http://dx.doi.org/10.1016/0021-9991(92)90240-Y.

Cao, J., 2005. Theoretical and experimental study of atomization from an annular liquid sheet. Proc. Inst. Mech. Eng. D 217 (8), 735–743. http://dx.doi.org/10.1243/09544070360692122.

Chatterjee, S., Das, M., Mukhopadhyay, A., Sen, S., 2015. Experimental investigation of breakup of annular liquid sheet in a hybrid atomizer. J. Propuls. Power 31 (5), 1232–1241. http://dx.doi.org/10.2514/1.B35574.

Chigier, N., Faragó, Z., 1992. Morphological classification of disintegration of round liquid jets in a coaxial air stream. At. Sprays 2 (2), 137–153. http://dx.doi.org/10.1615/AtomizSpr.v2.i2.50.

Choi, C.J., Lee, S.Y., 1997. Disintegration of annular liquid sheets with core air flow - mode classification. ICLASS (International Conf. Liq. At. Spray Systems) 24 (1–3), http://dx.doi.org/10.1615/InterJFluidMechRes.v24.i1-3.400.

Cifani, P., Michalek, W., Priems, G., Kuerten, J., van der Geld, C., Geurts, B., 2016. A comparison between the surface compression method and an interface reconstruction method for the VOF approach. Comput. & Fluids 136, 421–435. http://dx.doi.org/10.1016/j.compfluid.2016.06.026.

Deshpande, S.S., Anumolu, L., Trujillo, M.F., 2012. Evaluating the performance of the two-phase flow solver interfoam. Comput. Sci. Discov. 5 (1), 014016. http://dx.doi.org/10.1088/1749-4699/5/1/014016.

Dimotakis, P.E., 1986. Two-dimensional shear-layer entrainment. AIAA J. 24 (11), 1791–1796. http://dx.doi.org/10.2514/3.9525.

Dombrowski, N., Fraser, R.P., 1954. A photographic investigation into the disintegration of liquid sheets. Camb. Univ. Press 101–130. http://dx.doi.org/10.1098/rsta.1954.0014.

Duke, D., Honnery, D., Soria, J., 2012. Empirical scaling analysis of atomising annular liquid sheets. In: 12th Triennial International Conference on Liquid Atomization and Spray Systems.

Ibrahim, A.A., Jog, M.A., 2008. Nonlinear instability of an annular liquid sheet exposed to gas flow. Int. J. Multiph. Flow 34 (7), 647–664. http://dx.doi.org/10.1016/j.ijmultiphaseflow.2007.12.003.

Kendall, J.M., 1986. Experiments on annular liquid jet instability and on the formation of liquid shells. Phys. Fluids 29 (7), 2086. http://dx.doi.org/10.1063/1.865595.

Leboucher, N., Roger, F., Carreau, J.-L., 2010. Disintegration process of an annular liquid sheet assisted by coaxial gaseos coflow(s). At. Sprays 20, 847–862. http://dx.doi.org/10.1615/AtomizSpr.v20.i10.20.

Lefebvre, A., 1992. Twin-fluid atomization factors influencing mean drop size. At. Sprays 2, 101–119. http://dx.doi.org/10.1615/AtomizSpr.v2.i2.30.

Nicoud, F., Ducros, F., 1999. Subgrid-scale stress modelling based on the square of the velocity gradient tensor. Flow, Turbul. Combust. 62 (3), 183–200. http://dx.doi.org/10.1023/a:1009995426001.

OpenFOAM, 2023. Open source CFD toolbox. URL https://www.openfoam.com/news/main-news/openfoam-v2312.

Pope, S.B., 2000. Turbulent Flows, 12. print Cambridge Univ. Press, Cambridge.

Richter, J., Jakobs, T., Scheiff, F., Kolb, T., 2026. Classification of primary breakup modes for dual gas-assisted annular sheet nozzles. Int. J. Multiph. Flow 200, 105736. http://dx.doi.org/10.1016/j.ijmultiphaseflow.2026.105736.

Roenby, J., Bredmose, H., Jasak, H., 2016. A computational method for sharp interface advection. R. Soc. Open Sci. 3 (11), 160405. http://dx.doi.org/10.1098/rsos.160405.

Saeedipour, M., Schneiderbauer, S., 2021. Favre-filtered LES-vof of two-phase flows with eddy viscosity-based subgrid closure models: An a-posteriori analysis. Int. J. Multiph. Flow 144, 103780. http://dx.doi.org/10.1016/j.ijmultiphaseflow.2021.103780.

Sänger, A., 2018. Zerstäubung hochviskoser Fluide bei variierendem Systemdruck - Grundlagenforschung zur Hochdruck-Flugstromvergasung Dissertation. Karlsruher Institut für Technologie (KIT), Karlsruhe, http://dx.doi.org/10.5445/IR/1000087397.

Sänger, A., Jakobs, T., Djordjevic, N., Kolb, T., 2014. Effect of primary instability of a high viscous liquid jet on the spray quality generated by a twin-fluid atomizer.

Sänger, A., Jakobs, T., Kolb, T., 2016. Using primary instability analysis for determination of apparent liquid viscosity at jet breakup atomizing non-Newtonian fluids. In: 27th Annual Conference on Liquid Atomization and Spray Systems. http://dx.doi.org/10.5445/IR/1000062679.

Shen, J., Li, X., 1996. Breakup of annular viscous liquid jets in two gas streams. J. Propuls. Power 12 (4), 752–759. http://dx.doi.org/10.2514/3.24098.

Spalding, D.B., 1961. A single formula for the "Law of the Wall". J. Appl. Mech. 28 (3), 455–458. http://dx.doi.org/10.1115/1.3641728.

Stapper, B.E., Samuelsen, G.S., 1990. An experimental study of the breakup of a two-dimensional liquid sheet in the presence of co-flow air shear. In: AIAA – 28th Aerospace Sciences Meeting. http://dx.doi.org/10.2514/6.1990-461.

Strasser, W., 2011. Towards the optimization of a pulsatile three-stream coaxial airblast injector. Int. J. Multiph. Flow 37 (7), 831–844. http://dx.doi.org/10.1016/j.ijmultiphaseflow.2011.01.011.

Strasser, W., Battaglia, F., 2016. Identification of pulsation mechanism in a transonic three-stream airblast injector. J. Fluids Eng. 138 (11), 111303. http://dx.doi.org/10.1115/1.4033422.

Strasser, W., Battaglia, F., 2017a. The effects of prefilming length and feed rate on compressible flow in a self-pulsating injector. At. Sprays 27 (11), 929–947. http://dx.doi.org/10.1615/AtomizSpr.2017020111.

Strasser, W., Battaglia, F., 2017b. The effects of pulsation and retraction on non-Newtonian flows in three-stream injector atomization systems. Chem. Eng. J. 309, 532–544. http://dx.doi.org/10.1016/j.cej.2016.10.046.

Strasser, W., Battaglia, F., 2018. Pulsating slurry atomization, film thickness, and azimuthal instabilities. At. Sprays 28 (7), http://dx.doi.org/10.1615/AtomizSpr.2018026380.

Strasser, W., Tilbrook, A., Wilson, D.M., 2026. Spontaneous axis-switching swirling in transonic core-annular flow of highly differentiated fluids. Transp. Phenom. 1 (1), http://dx.doi.org/10.1515/tp-2026-0012.

Sun, Y., Hasse, C., Sadiki, A., 2025. Large eddy simulation based seamless VOF-LPT approach for describing atomization and evaporation processes: Application to jets in crossflow. Int. J. Heat Mass Transfer 242, 126807. http://dx.doi.org/10.1016/j.ijheatmasstransfer.2025.126807.

Tian, X.-S., Zhao, H., Liu, H.-F., Li, W.-F., Xu, J.-L., 2014. Effect of central tube thickness on wave frequency of coaxial liquid jet. Fuel Process. Technol. 119, 190–197. http://dx.doi.org/10.1016/j.fuproc.2013.11.011.

Wachter, S., Jakobs, T., Kolb, T., 2021. Comparison of central jet and annular sheet atomizers at identical gas momentum flows. Ind. Eng. Chem. Res. 60 (30), 11502–11512. http://dx.doi.org/10.1021/acs.iecr.1c01526.

Wahono, S., Honnery, D., Soria, J., Ghojel, J., 2008. High-speed visualisation of primary break-up of an annular liquid sheet. Exp. Fluids 44 (3), 451–459. http://dx.doi.org/10.1007/s00348-007-0361-8.

Zhang, F., Wachter, S., Zirwes, T., Jakobs, T., Zarzalis, N., Trimis, D., Kolb, T., Stapf, D., 2023. Effect of nozzle upscaling on coaxial, gas-assisted atomization. Phys. Fluids 35 (4), http://dx.doi.org/10.1063/5.0141156.

Zhang, F., Zirwes, T., Müller, T., Wachter, S., Jakobs, T., Habisreuther, P., Zarzalis, N., Trimis, D., Kolb, T., 2020. Effect of elevated pressure on air-assisted primary atomization of coaxial liquid jets: Basic research for entrained flow gasification. Renew. Sustain. Energy Rev. 134 (3), 110411. http://dx.doi.org/10.1016/j.rser.2020.110411.

Zhao, H., Wu, Z.-W., Li, W.-F., Xu, J.-L., Liu, H.-F., 2018. Nonmonotonic effects of aerodynamic force on droplet size of prefilming air-blast atomization. Ind. Eng. Chem. Res. 57 (5), 1726–1732. http://dx.doi.org/10.1021/acs.iecr.7b05026.